The Astrophysical Journal Letters, 972:L13 (13pp), 2024 September 1 https://doi.org/10.3847/2041-8213/ad6c32

Discovery of a Relativistic Stripped-envelope Type Ic-BL Supernova at $z = 2.83$ with JWST

M. R. Siebert[1], C. DeCoursey[2], D. A. Coulter[1], M. Engesser[1], J. D. R. Pierel[1,17], A. Rest[1,3], E. Egami[2], M. Shahbandeh[1], W. Chen[4], O. D. Fox[1], Y. Zenati[1,3,18], T. J. Moriya[5,6,7], A. J. Bunker[8], P. A. Cargile[9], M. Curti[10], D. J. Eisenstein[9], S. Gezari[1], S. Gomez[1], M. Guolo[3], B. D. Johnson[9], B. A. Joshi[3], M. Karmen[3], R. Maiolino[11,12,13], R. M. Quimby[14,15], B. Robertson[16], L. G. Strolger[1], F. Sun[9], Q. Wang[3], and T. Wevers[1]
[1] Space Telescope Science Institute, Baltimore, MD 21218, USA; msiebert@stsci.edu
[2] Steward Observatory, University of Arizona, 933 North Cherry Avenue, Tucson, AZ 85721, USA
[3] Physics and Astronomy Department, Johns Hopkins University, Baltimore, MD 21218, USA
[4] Department of Physics, Oklahoma State University, 145 Physical Sciences Building, Stillwater, OK 74078, USA
[5] National Astronomical Observatory of Japan, National Institutes of Natural Sciences, 2-21-1 Osawa, Mitaka, Tokyo 181-8588, Japan
[6] Graduate Institute for Advanced Studies, SOKENDAI, 2-21-1 Osawa, Mitaka, Tokyo 181-8588, Japan
[7] School of Physics and Astronomy, Monash University, Clayton, VIC 3800, Australia
[8] Department of Physics, University of Oxford, Denys Wilkinson Building, Keble Road, Oxford OX1 3RH, UK
[9] Center for Astrophysics | Harvard & Smithsonian, 60 Garden Street, Cambridge, MA 02138, USA
[10] European Southern Observatory, Karl-Schwarzschild-Strasse 2, 85748 Garching, Germany
[11] Kavli Institute for Cosmology, University of Cambridge, Madingley Road, Cambridge CB3 0HA, UK
[12] Cavendish Laboratory, University of Cambridge, 19 JJ Thomson Avenue, Cambridge CB3 0HE, UK
[13] Department of Physics and Astronomy, University College London, Gower Street, London WC1E 6BT, UK
[14] Department of Astronomy/Mount Laguna Observatory, San Diego State University, 5500 Campanile Drive, San Diego, CA 92812-1221, USA
[15] Kavli Institute for the Physics and Mathematics of the Universe (WPI), The University of Tokyo Institutes for Advanced Study, The University of Tokyo, Kashiwa, Chiba 277-8583, Japan
[16] Department of Astronomy and Astrophysics, University of California, Santa Cruz, 1156 High Street, Santa Cruz, CA 96054, USA
Received 2024 June 7; revised 2024 July 22; accepted 2024 July 22; published 2024 August 26

Abstract

We present James Webb Space Telescope (JWST) NIRCam and NIRSpec observations of a Type Ic supernova (SN Ic) and its host galaxy (JADES-GS+53.13533-27.81457) at $z = 2.83$. This SN (named SN 2023adta) was identified in deep JWST/NIRCam imaging from the JWST Advanced Deep Extragalactic Survey (JADES) program. Follow-up observations with JWST/NIRSpec provided a spectroscopic redshift of $z = 2.83$ and the classification as an SN Ic-BL. The light curve of SN 2023adta matches well with other stripped-envelope SNe, and we find a high peak luminosity, $M_V = -19.0 \pm 0.2$ mag, based on the distribution of best-fit SNe. The broad absorption features in its spectrum are consistent with other SNe Ic-BL 1–3 weeks after peak brightness. We measure a Ca II near-IR triplet expansion velocity of $29{,}000 \pm 2000$ km s^{-1}. The host galaxy of SN 2023adta is irregular, and modeling of its spectral energy distribution indicates a metallicity of $Z = 0.35^{+0.16}_{-0.08} Z_{\odot}$. This environment is consistent with the population of low-z SNe Ic-BL that prefer lower metallicities relative to other stripped-envelope SNe and track long-duration γ-ray burst environments. We do not identify any γ-ray bursts that are coincident with SN 2023adta. Given the rarity of SNe Ic-BL in the local Universe, the detection of an SN Ic-BL at $z = 2.83$ could indicate that their rates are enhanced at high redshift.

Unified Astronomy Thesaurus concepts: Supernovae (1668); Core-collapse supernovae (304); Type Ic supernovae (1730)

1. Introduction

Stripped-envelope supernovae (SESNe) result from the core collapse of massive stars that have experienced some form of mass loss causing them to lose their outer layers of hydrogen and sometimes helium (Clocchiatti et al. 1996). A Type Ic supernova (SN Ic) is an SESN characterized by the lack of both H and He features in its spectra (Filippenko et al. 1995; Matheson et al. 2001) and requires a progenitor star that has experienced a large amount of stripping (see Woosley et al. 1994; Dessart et al. 2012, 2020; Gal-Yam 2017). Two primary channels with different mass-loss mechanisms are thought to be able to produce an SN Ic. The first is the collapse of a high-mass Wolf–Rayet (W-R) star (Woosley & Weaver 1995; Georgy et al. 2009), whose strong metal-line-blanketing-driven winds have removed its outer layers. Progenitor angular momentum and metallicity likely play an important role in these progenitors because they result in stronger stellar winds. The second channel consists of young massive stars in close binary systems whose mass loss occurs through Roche-lobe overflow or common-envelope evolution (Podsiadlowski et al. 1992; Yoon et al. 2010; Sana et al. 2012; Lyman et al. 2016). It is important to note that these channels are not mutually exclusive, and a combination of both mass-loss mechanisms is likely needed to explain the diversity of SESNe (Smith et al. 2015).

There have been limited searches to directly detect companion stars. To date, there are only two SNe Ic nearby enough to detect any potential companion. Deep postexplosion

[17] NASA Einstein Fellow.
[18] ISEF International Fellowship.

upper limits of the Type Ic SN 1994I, which had earlier data restricting any single-star scenario, favored companion scenarios with nonconservative mass transfer with intermediate initial orbital periods and mass ratios (Van Dyk et al. 2016). Deep postexplosion observations of the fully stripped Type Ib/c SN 2013ge resulted in a direct detection of a surviving companion consistent with a slightly reddened post-main-sequence 12 $M_{\odot}$ star (Fox et al. 2022). Aside from these two postexplosion observations, preexplosion spectral energy distributions (SEDs) and detailed modeling suggest potential companions in the Type Ib iPTF13bvn (e.g., Cao et al. 2013; Eldridge & Maund 2016; Folatelli et al. 2016), Ib 2019yvr (Kilpatrick et al. 2021; Sun et al. 2022), and Ic 2020oi (Gagliano et al. 2022), although none of these have been confirmed with postexplosion imaging.

Broad-line SNe Ic (SNe Ic-BL) are a rare subclass of the Type Ic events, exhibiting broad spectral features that indicate unusually high ejecta velocities of ~20,000–30,000 km s^{-1}(~0.1c; Galama et al. 1998; Modjaz et al. 2006, 2016; Sahu et al. 2018; Taddia et al. 2019). Additionally, the luminosities of these SNe are typically higher than those of other core-collapse SNe (Drout et al. 2011; Cano 2013; Taddia et al. 2019). Models suggest that the kinetic energy of these explosions can be as high as 10^{52} erg (Mazzali et al. 2002; Maeda et al. 2003; Janka et al. 2016; Prentice et al. 2016), which is a factor of 10 larger than other typical SNe. Furthermore, SNe Ic-BL are the only SN type to be associated with long-duration γ-ray bursts (LGRBs), whose γ-ray emission lasts longer than 2 s (Galama et al. 1998; Woosley & Bloom 2006; Modjaz et al. 2016, 2020). Iwamoto et al. (1999) showed that these SNe can also be accompanied by X-ray flashes, which further suggests that only SNe Ic-BL are associated with LGRBs.

LGRBs are considered to be a natural result of the collapsar model for SESNe (Woosley & MacFadyen 1999). In this progenitor scenario, the core of a massive star collapses to create a rapidly rotating compact object, then accretion onto this compact object utilizes the rotational energy of the star via magnetic coupling and launches collimated jets that power the explosion and produce the GRB (Woosley 1993; Woosley & MacFadyen 1999). The absence of LGRBs and/or their associated afterglows in normal SNe Ib/c disfavors the collapsar theory for explaining these SNe and challenges the connection between normal SNe Ic and SNe Ic-BL (see Corsi et al. 2012; Barnes et al. 2018; Modjaz et al. 2020; Zenati et al. 2020). Many SNe Ic-BL, however, are observed without an associated LGRB, and the reason for this is not fully understood.

Other progenitor channels for SNe Ic-BL may be possible. Zapartas et al. (2017) provide a detailed analysis of deep, postexplosion upper limits of the Type Ic-BL SN 2002ap. The SN progenitor has a low metallicity and high ejecta mass, ruling out most single-star models. Instead, the deep upper limits, when combined with the explosion parameters of the primary star, suggest a more likely scenario consisting of a low-mass binary system in an eccentric orbit undergoing nonconservative mass transfer. Another more exotic, but tempting, possibility for SN 2002ap is a reverse merger of the companion star with the compact remnant from the primary explosion.

The results for SN 2002ap suggest a possible bimodality in the progenitor population of SNe Ic-BL, but one important avenue for understanding the progenitors of SESNe and the connection between SNe Ic-BL and LGRBs is through detailed analysis of their environments. Theory predicts that metallicity should play an important role in the production of LGRBs. Specifically, Woosley & Bloom (2006) suggested that angular momentum loss due to the metal-line-driven winds in a W-R star could prohibit the formation of a compact object that was rotating fast enough to launch a jet. Therefore, they proposed a metallicity threshold of $Z < 0.3\ Z_{\odot}$ for collapsars.

Several studies have confirmed that SNe Ic-BL prefer lower-metallicity environments relative to other core-collapse SNe (Kelly & Kirshner 2012; Sanders et al. 2012; Arcavi 2018; Modjaz et al. 2020). In particular, Modjaz et al. (2020) found that SNe Ic-BL with and without associated GRBs prefer statistically similar environments with low metallicity and high specific star formation rates. Modjaz et al. (2020) conclude that SNe Ic-BL without GRBs in their sample produced either jets that were choked within the star (Milisavljevic et al. 2015; Modjaz et al. 2016) or off-axis GRBs. Nonetheless, it is still debated whether metallicity is required to explain the presence of a jet (Mannucci et al. 2011).

The clear connection between SESN type and the host environment suggests that metallicity could be a key factor in discerning their progenitor scenarios. Observing SESNe at high z presents an opportunity to study their properties in a diversity of environments. At high z, there is more access to very low-metallicity environments ($Z < 0.1\ Z_{\odot}$) like those present in local metal-poor dwarf galaxies. So far, only a small sample of low-z core-collapse SNe have been studied in extreme environments like these (Arcavi et al. 2010; Taddia et al. 2016; Anderson et al. 2018; Gutiérrez et al. 2018; Tucker et al. 2024). Given the rarity of SNe Ic-BL, we do not yet know if a population of these SNe exists in very low-metallicity environments. If the environments of SNe Ic-BL deviate from the LGRB population at high z, it may indicate that multiple progenitor scenarios are required to explain these SNe. Furthermore, we can constrain how their observational properties and rates may evolve with redshift.

In this work, we present James Webb Space Telescope (JWST) NIRCam and NIRSpec observations of SN 2023adta. This SN was identified in the JWST Advanced Deep Extragalactic Survey (JADES; Eisenstein et al. 2023). A JWST Director's Discretionary Time (DDT) program was accepted to follow up the most interesting transients ($1 < z < 4$) in this field with additional NIRCam photometry and NIRSpec spectroscopy (DeCoursey et al. 2024, hereafter D24). Details on the sample of high-z SNe and the design of the JADES Transient Survey + DDT observations are presented in the companion paper.

In combination with the resulting light curve from these data, we used the NIRSpec Prism spectrum of SN 2023adta (covering 0.6–5.3 μm at $R \sim 100$) to confirm its redshift ($z = 2.83$) and classify it as an SN Ic-BL. To date, this is the highest-redshift SESN ever discovered. We also determine that it came from a low-metallicity environment that is consistent with low-z analogs.

In Section 2, we summarize our observations; in Section 3, we describe the observational properties of SN 2023adta (and its host galaxy), discuss its classification as an SN Ic-BL, and put it into the context of other local SESNe; and in Section 4, we summarize our findings and their implications and discuss future observations. In all subsequent analysis, we assume a

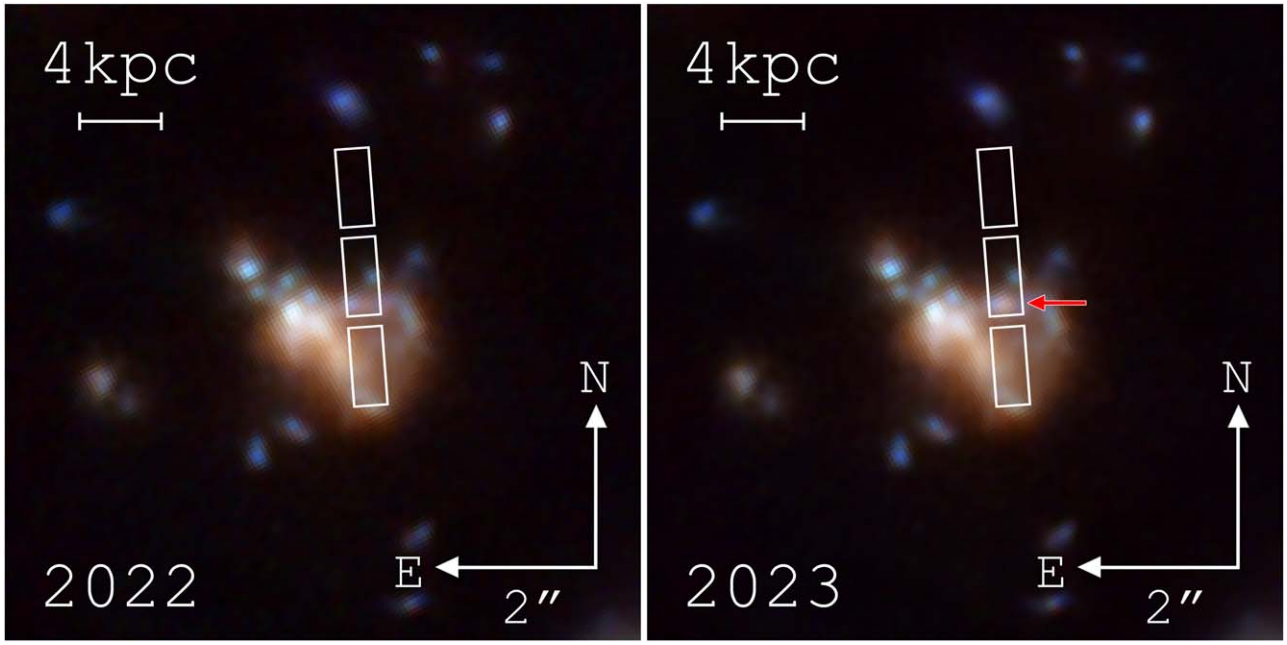

Figure 1. False-color images of SN 2023adta and its host galaxy taken in 2022 (left) and 2023 (right). The white rectangles show the orientation of the MSA three-shutter slitlet on the sky. Two additional nodded exposures were acquired north and south of this central location. The SN (indicated by the red arrow) is located near the southern edge of the central slit.

standard ΛCDM cosmology with $H_0 = 70\,\mathrm{km\,s^{-1}\,Mpc^{-1}}$ and $\Omega_m = 0.315$.

2. Observations and Data Reduction

A detailed description of the JADES transient observing program methods and data reduction is presented in D24. In short, JADES observations were taken over a 1 yr time baseline from 2022 September to 2024 January, allowing us to conduct a transient search of unprecedented 5σ $m_{\mathrm{AB}} \sim 30$ depth. The first observing window was between 2022 September 29 and October 5, and the second epoch took place between 2023 September 29 and October 3 with an overlap of $25'^2$ in the NIRCam F090W, F115W, F150W, F200W, F277W, F335M, F356W, F410M, and F444W filters. Additional visits on 2023 November 15 and 2024 January 1 were performed due to failed observations.

A JWST DDT program was approved to follow and classify the most interesting transients with two additional NIRCam visits on 2023 November 28 and 2024 January 1. The second visit included the NIRSpec multiobject spectroscopy (MOS) mode using the microshutter assembly (MSA) and Prism ($R \sim 100$) grating. The MSA provided SN spectra for ∼10 transients, some of which are described in companion papers (e.g., Pierel et al. 2024a; D. A. Coulter et al. 2024, in preparation; E. Egami et al. 2024, in preparation), as well as a variety of galaxy spectra. In this section, we describe the data products and reduction methods for SN 2023adta.

2.1. JWST NIRCam

Our data reduction methods are described in detail by D24, but we summarize the process here. We adopt the point-spread function (PSF) fitting method developed in Pierel et al. (2024b) for measuring photometry on Level 3 (drizzled and resampled 2D data) JWST images. Unlike their scenario, though, we have a template image for all epochs of SN 2023adta from the 2022 JADES observations. We therefore first align the Level 2 (CAL) NIRCam images containing SN 2023adta to the template images (in each filter) using the JWST/HST Alignment Tool (Rest et al. 2023)[19] software and then produce aligned Level 3 images with the JWST pipeline (v 1.12.5; Bushouse et al. 2024, and see Figure 1). We obtain difference images in all filters using the High Order Transform of PSF and Template Subtraction (Becker 2015)[20] code and then implement the Level 3 PSF fitting routine from Pierel et al. (2024b) using 5×5 pixel cutouts and Level 2 PSF models from `webbpsf`,[21] which are temporally and spatially dependent and include a correction to the infinite aperture flux. The Level 2 PSF models are drizzled to create a Level 3 PSF model consistent with the observations. The total measured fluxes, which are in units of MJy $\mathrm{sr^{-1}}$, are converted to AB magnitudes using the native pixel scale of each image ($0.''03\,\mathrm{pixel^{-1}}$ for short wavelength, $0.''06\,\mathrm{pixel^{-1}}$ for long wavelength). Measured photometry is given in Table 1.

2.2. JWST Spectroscopy

SN 2023adta (R.A. $= 3^{\mathrm{h}}32^{\mathrm{m}}32\overset{\mathrm{s}}{.}4657$, decl. $= -27^{\mathrm{d}}48^{\mathrm{m}}52\overset{\mathrm{s}}{.}2371$) was selected as one of the highest-priority targets for spectroscopic follow-up observations because of its brightening in 2023 November 28 images (F200W = 26.5 mag) relative to the discovery image taken on 2022 October 1 (F200W = 28.5 mag). We observed SN 2023adta on 2024 January 1 with the JWST MSA (Ferruit et al. 2022) and NIRSpec Prism (observation details in Table 2). Three nodded exposures were acquired using three-shutter slitlets centered on each target in the MSA design. This observing pattern results in five unique shutter locations

[19] https://jhat.readthedocs.io
[20] https://github.com/acbecker/hotpants
[21] https://webbpsf.readthedocs.io

Table 1
Photometry for SN 2023adta Measured in Section 2.1

PID	Instrument	MJD	Filter/Disperser	m_{AB}
1180	NIRCam	60220	F090W	>30.2
1180	NIRCam	60220	F115W	29.65 ± 0.11
1180	NIRCam	60220	F150W	29.11 ± 0.09
1180	NIRCam	60220	F200W	28.54 ± 0.08
1180	NIRCam	60220	F277W	28.91 ± 0.10
1180	NIRCam	60220	F335M	28.60 ± 0.13
1180	NIRCam	60220	F356W	28.69 ± 0.10
1180	NIRCam	60220	F410M	29.19 ± 0.22
1180	NIRCam	60220	F444W	29.31 ± 0.22
1180	NIRCam	60264	F090W	>29.9
1180	NIRCam	60264	F115W	29.73 ± 0.19
1180	NIRCam	60264	F150W	27.45 ± 0.06
1180	NIRCam	60264	F200W	26.53 ± 0.04
1180	NIRCam	60264	F277W	26.64 ± 0.04
1180	NIRCam	60264	F335M	26.52 ± 0.04
1180	NIRCam	60264	F356W	26.74 ± 0.04
1180	NIRCam	60264	F410M	26.86 ± 0.06
1180	NIRCam	60264	F444W	27.07 ± 0.06
6541	NIRCam	60276	F115W	>28.9
6541	NIRCam	60276	F150W	27.63 ± 0.09
6541	NIRCam	60276	F200W	26.55 ± 0.05
6541	NIRCam	60276	F277W	26.57 ± 0.05
6541	NIRCam	60276	F356W	26.59 ± 0.06
6541	NIRCam	60276	F444W	26.92 ± 0.08
6541	NIRCam	60310	F150W	28.44 ± 0.14
6541	NIRCam	60310	F200W	26.98 ± 0.05
6541	NIRCam	60310	F277W	26.88 ± 0.07
6541	NIRCam	60310	F356W	26.69 ± 0.06
6541	NIRCam	60310	F444W	26.94 ± 0.09
6541	NIRSpec	60310	Prism	⋯
1180	NIRCam	60311	F090W	>29.4
1180	NIRCam	60311	F115W	>29.9
1180	NIRCam	60311	F150W	28.85 ± 0.10
1180	NIRCam	60311	F200W	27.01 ± 0.04
1180	NIRCam	60311	F277W	26.79 ± 0.04
1180	NIRCam	60311	F335M	26.42 ± 0.04
1180	NIRCam	60311	F356W	26.63 ± 0.04
1180	NIRCam	60311	F410M	26.57 ± 0.05
1180	NIRCam	60311	F444W	26.79 ± 0.05

Note. Upper limits are 5σ.

(each $0\farcs46 \times 0\farcs20$) open to the sky around each target. We show the orientation of the central three-shutter slitlet for SN 2023adta in Figure 1. This orientation allowed for the independent extractions of SN 2023adta and part of its extended host galaxy.

We reduced the JWST data using the "jwst"[22] pipeline (version 1.14.0; Bushouse et al. 2024) routines for bias and dark subtraction, background subtraction, flat-field correction, wavelength calibration, flux calibration, rectification, outlier detection, and resampling. Given that the host galaxy is extended and its flux falls within multiple shutters, the default nodded point-source background subtraction method is not sufficient for this target. Therefore, we reran Stage 2 of the pipeline (calwebb_spec2) using the master background subtraction strategy, which makes use of designated background

[22] https://github.com/spacetelescope/jwst

Table 2
JWST SN 2023adta NIRSpec Observation Details

Setting	Value
Instrument	NIRSpec
Mode	MOS
Wavelength range	0.6–5.3 μm
Slit	Three-shutter ($0\farcs46 \times 0\farcs2$ each)
Grating/filter	Prism/CLEAR
$R = \lambda/\Delta\lambda$	∼30–300
Readout pattern	NRSIRS2
Groups per integration	19
Integrations per exposure	2
Exposures/nods	3
Total exposure time	16,631 s

shutters. We performed manual interactive extractions of both SN 2023adta and its host galaxy from the 2D Stage 2 data product using the Specviz module of Jdaviz.[23] Since the resolution of the Prism is nonlinear with wavelength ($R \sim 30$–300; Jakobsen et al. 2022), we use an irregularly spaced wavelength grid with $\Delta\lambda$ in the range 34–201 Å.

Some details of our data reduction choices and results are shown in Figure 2. In the top panel, we show the 2D, master-background-subtracted NIRspec Prism spectrum of SN 2023adta and its host galaxy. The color map has units of MJy sr^{-1}. The trace of SN 2023adta is shown by the dashed blue horizontal line, and the trace of the host galaxy is indicated by the dashed pink horizontal line and located $0\farcs4$ south of SN 2023adta. Using the Specviz module of JDaviz (Developers et al. 2023), we perform a boxcar extraction with 3 pixel width on both of these traces.

We flux calibrate the host galaxy spectrum in two different ways. First, we scale the spectrum to the 2022 host galaxy photometry[24] (well before the SN explosion; Eisenstein et al. 2023). We use this spectrum as input for the SED fitting code `BAGPIPES`[25] (Carnall et al. 2018, 2019) to derive an initial redshift and the host galaxy parameters presented in Section 3.4. Second, we scale the original extracted host spectrum to the 2022 host galaxy photometry measured at the SN position in order to get an estimate of the underlying host galaxy flux. We do something similar for the extracted spectrum of SN 2023adta but instead scale to the NIRCam photometry observed at the same epoch. The flux-calibrated spectra of SN 2023adta and its host galaxy (SN position estimate) are shown in the middle panel of Figure 2 (blue and pink curves, respectively), and the difference between them is shown in the bottom panel (black).

Clear, narrow host galaxy emission from [O II], [O III], Hα, and [S III] is present in the spectrum of SN 2023adta (marked with dashed vertical lines). The host galaxy exhibits a strong Balmer break (1.5 μm observer frame) and has notably weaker emission lines relative to the continuum than what is present in the spectrum of SN 2023adta. We expect that our measured host galaxy continuum flux (determined from the extended emission in the southernmost shutter) should be a reasonable estimate for what is underlying the SN. However, we note that the SN is $0\farcs1$ from a region of star formation whose flux also contributes to our SN spectrum (see Figure 1). This could be

[23] https://jdaviz.readthedocs.io/en/latest/specviz/index.html
[24] JADES Host ID 198373 from https://archive.stsci.edu/hlsp/jades.
[25] https://bagpipes.readthedocs.io/en/latest/

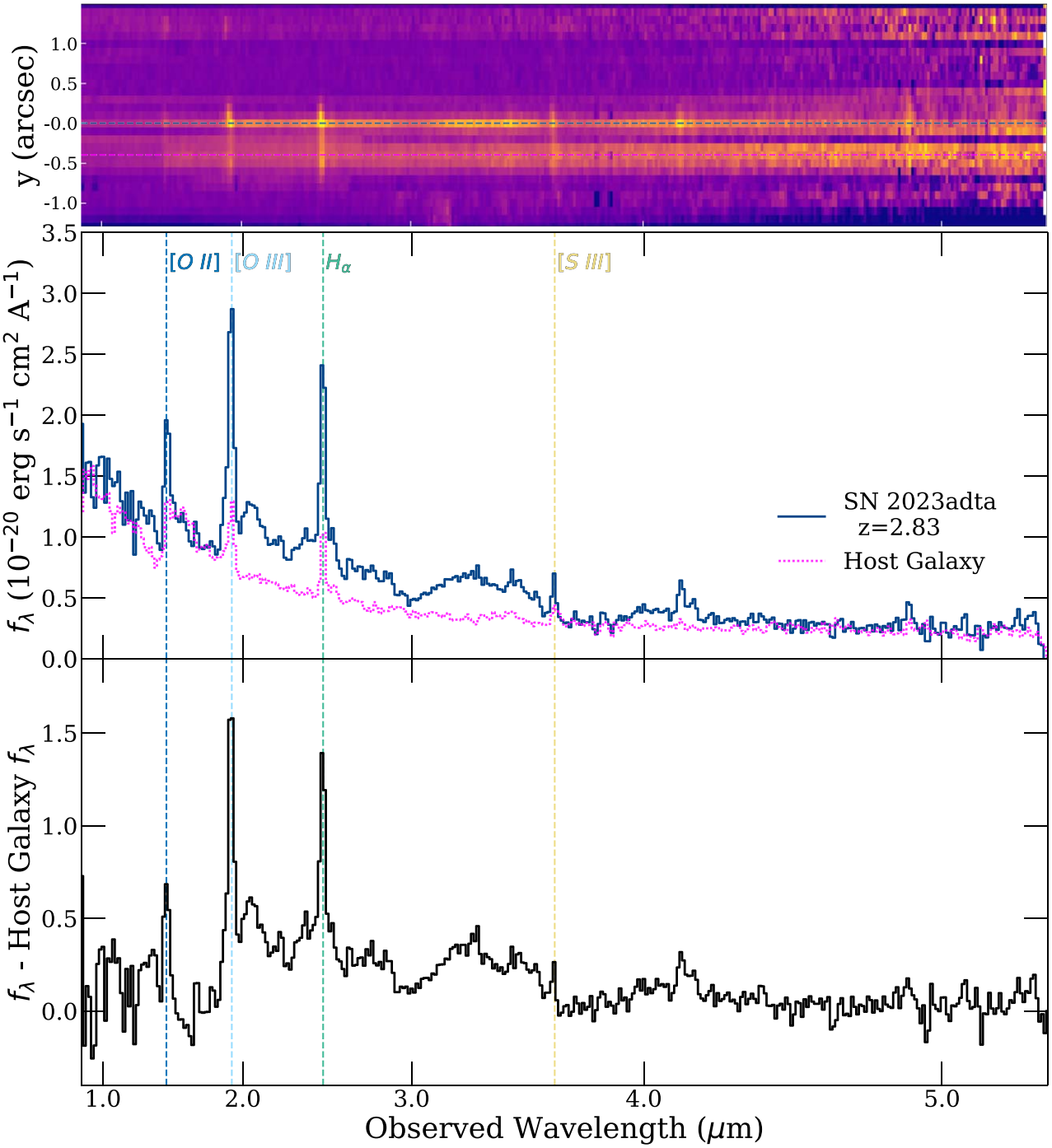

Figure 2. (Top) The 2D, master-background-subtracted, NIRSpec Prism spectrum of SN 2023adta and its host galaxy in MJy sr^{-1}. As shown in Figure 1, our observations capture both the SN and part of its host galaxy. The central rows for the extraction of SN 2023adta and its host galaxy are noted by the dashed blue and pink horizontal lines, respectively. (Middle) The resulting 1D extractions of SN 2023adta (blue) and its host galaxy (pink) in flux converted to f_λ. The spectrum of SN 2023adta was scaled to its photometry at the same epoch, and the spectrum of the host galaxy was scaled to the 2022 photometry at the position of the SN with an identical $0\farcs1$ aperture. Notable narrow emission lines from the host galaxy are marked with the dashed vertical lines. (Bottom) The difference between the flux-calibrated SN and host galaxy spectra from the middle panel. Assuming the host galaxy emission underlying the SN is similar to the galaxy emission at our extracted location, this spectrum should be mostly isolated SN flux. However, the presence of narrow emission lines could indicate that this subtraction is imperfect.

the reason for the imperfect subtraction of the host galaxy emission lines.

The difference spectrum should contain mostly isolated SN flux. In this final spectrum of SN 2023adta, we see broad absorption features at 3.0 μm and 3.7 μm. We analyze these features in more detail in Section 3.2.

2.3. Redshift and Host Galaxy

SN 2023adta was identified in host galaxy JADES-GS +53.13533-27.81457. We fit the NIRspec Prism data of the host galaxy using the SED fitting code `BAGPIPES` (Carnall et al. 2018, 2019) to determine an initial redshift estimate ($z = 2.83$). We then further refine this estimate by fitting

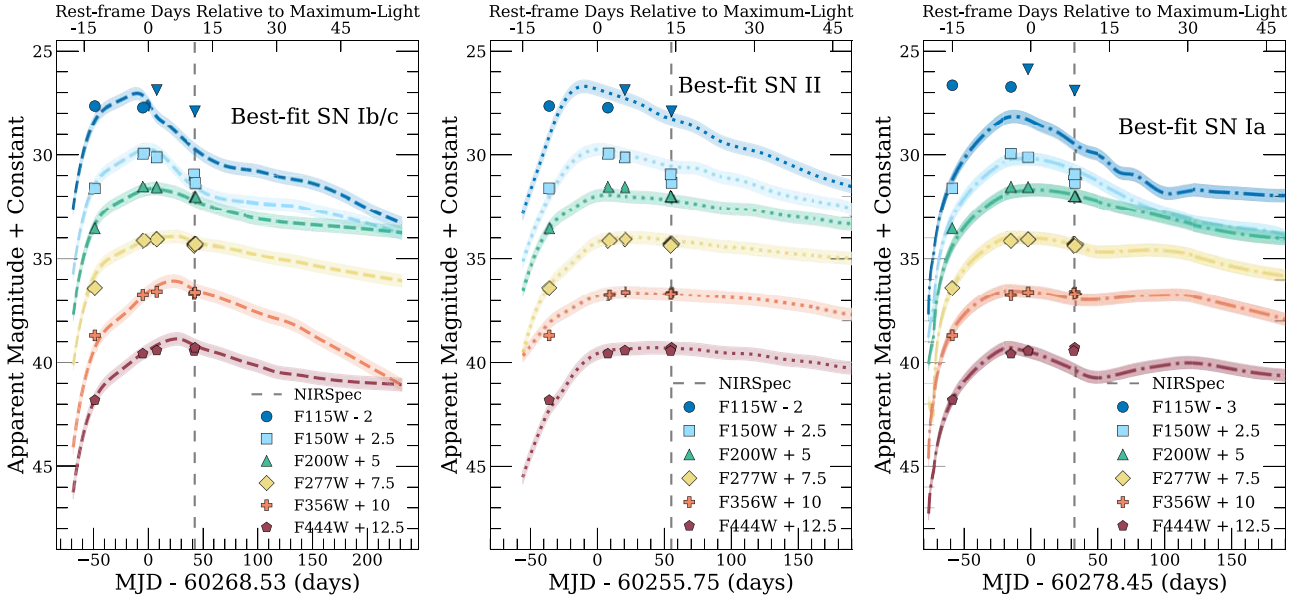

Figure 3. (Left) The multiband light curve of SN 2023adta (colored points), plotted with the offsets shown for visual clarity, and its best-matched SN Ib/c light curve (dashed curves). The epoch of our NIRSpec Prism spectrum is marked with the dashed vertical line and indicates an approximate phase of +11 days relative to peak brightness in F150W . (Middle) Similar to the left panel but showing the best-fit SN II. (Right) Similar to the other panels but showing the best-fit SN Ia SALT3-NIR model (Pierel et al. 2022) with shape and color parameters of $x_1 = -0.29$ and $c = 0.63$, respectively.

Table 3
Best-fit Light-curve Parameters and Properties for SN 2023adta

Parameter	Bounds	SN Ib/c	SN II	SN Ia
z	Fixed	$z = 2.83$	$z = 2.83$	$z = 2.83$
t_{pk}	[60120, 60411]	60270.09 ± 0.32	60255.75 ± 0.51	60278.45 ± 0.41
A	$[0, 6 \times 10^{-18}]$	$(4.86 \pm .05) \times 10^{-19}$	$(2.73 \pm .03) \times 10^{-19}$	...
M_V	...	19.0 ± 0.2[a]	19.4 ± 0.3[a]	19.03 ± 0.03
Host $E(B-V)$	[0, 3]	$(1.17 \pm 4) \times 10^{-3}$	0.43 ± 0.0006	...
Host R_V	[2, 4]	2.92 ± 0.08	2.03 ± 0.05	...
x_0	$[0, 3 \times 10^{-6}]$	...	...	$(5.92 \pm 0.05) \times 10^{-8}$
x_1	[−3, 3]	...	...	-0.29 ± 0.08
c	[−1.5, 1.5]	...	...	0.63 ± 0.02
χ^2/ν	...	1.00 (1.6 ± 0.4)[a]	1.56 (2.4 ± 0.5)[a]	1.75

Note.
[a] Mean and standard deviation for the 10 best-fit SNe of this type.

individual emission lines present in the spectrum following the methods of Bunker et al. (2023). At this redshift, several galaxy emission lines blended together. We model Hα+N II and [S II] $\lambda\lambda$6716, 6731 as individual Gaussian components. We fit Hα+N II and [S II] $\lambda\lambda$6716, 6731 simultaneously with their centroids fixed relative to one another and do something similar for [O III] $\lambda\lambda$4959, 5007. Using these gas-phase nebular emission lines, we measure a final redshift of $z = 2.830 \pm 0.001$. This uncertainty is consistent with those measured for Prism spectra in Bunker et al. (2023; $\Delta z = 0.001$–0.01 at $z = 2.83$). For a detailed analysis of the properties of the host galaxy of SN 2023adta, see Section 3.4.

3. Analysis

3.1. Light Curve

We examine the light curve of SN 2023adta (originally presented in D24) in Figure 3. The data shown (colored points) are NIRCam wideband photometry. We fit the observed photometry using all existing core-collapse SN light-curve evolution models with rest-frame optical to near-IR (NIR; to observer frame $\sim$4 μm) wavelength coverage (Pierel et al. 2018) and the SALT3-NIR SN Ia light-curve model (Pierel et al. 2022). Prior to fitting, we correct for Galactic extinction ($E(B-V) = 0.01$ mag with $R_V = 3.1$). In Figure 3, we show the best-fit SN Ib/c model, SN II model, and SALT3-NIR SN Ia model from left to right. The epoch of our NIRSpec DDT observation is represented by the vertical dashed line. For the SN Ib/c model, this occurs at a phase of +11 days relative to peak brightness in F150W (+14 days and +8 days for the SN II and SN Ia models, respectively). For the SN Ia model, we find the best-fit shape and color parameters of $x_1 = -0.29$ and $c = 0.63$, respectively. The core-collapse light-curve models do not have uncertainties. Therefore, to determine the relative goodness of fit, we add a constant uncertainty to each model light curve such that $\chi^2/\nu = 1.0$ for the best fit (SN Ib/c). We add identical uncertainty to the SN II and SALT3-NIR SN Ia models so that the χ^2/ν values are directly comparable. This uncertainty is shown by the shaded regions in Figure 3. The model parameters for each fit are shown in Table 3.

We find that SESNe reproduce the multiband light-curve evolution of SN 2023adta. Specifically, from each of the top 10

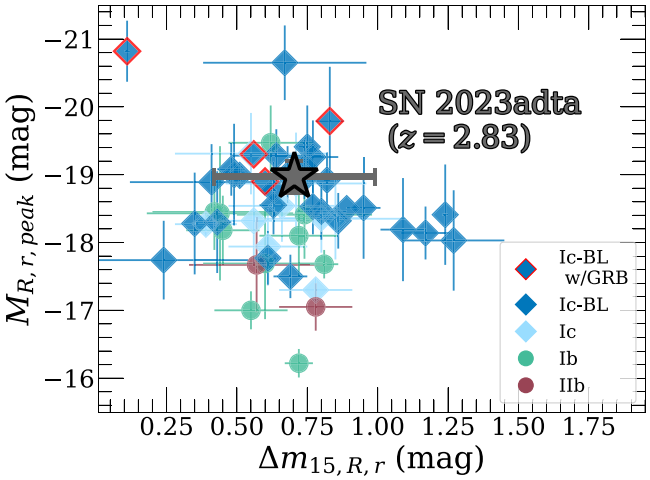

Figure 4. Comparison of the light-curve peak brightness ($M_{R,r}$) and shape ($\Delta m_{15,R,r}$) characteristics of SN 2023adta to other SESNe from Drout et al. (2011) and SNe Ic-BL from Taddia et al. (2019). Measurements were derived from *R*- and *r*-band photometry, respectively.

core-collapse SN Ib/c and SN II fits, we determine $\chi^2/\nu = 1.6 \pm 0.4$ and 2.4 ± 0.5 for each SN type, respectively. The best-fit SN Ia model has $\chi^2/\nu = 1.75$. While all fits perform well in the rest-frame optical (F150W, F200W, F277W, and F356W), the best-fit SN Ia is unable to reproduce the flux at rest-frame near-UV wavelengths (F115W). The best-fit SN Ib/c and SN II are also better matched to the last epoch in F444W. Due to the limitations of the data, we caution that the light-curve models are most uncertain at the reddest wavelengths. If we assume $H_0 = 70\ \mathrm{km\ s^{-1}\ Mpc^{-1}}$ (Riess et al. 2016, 2018), we find a high peak luminosity of $M_V = -19.0 \pm 0.2$ mag ($M_R = -19.1 \pm 0.2$ mag) for the SN Ib/c model. We note that the best-fit SN II models similarly require high peak brightnesses ($M_V = -19.4 \pm 0.3$ mag) that are difficult to reconcile with the observed luminosity functions of normal SN II (Li et al. 2011; Valenti et al. 2016). Similar to χ^2/ν, we derive these uncertainties from the distribution of the 10 best-fit SN Ib/c models.

Some studies have shown that SN Ic-BL light curves are very similar to those of other SNe Ib/c but tend toward higher absolute luminosities (Drout et al. 2011; Taddia et al. 2015; Lyman et al. 2016; Prentice et al. 2016). In particular, Drout et al. (2011) found a mean $M_{R,\mathrm{peak}} = -19.0 \pm 1.1$ mag for SNe Ic BL ($M_{R,\mathrm{peak}} = -17.9 \pm 0.9$ mag and -18.3 ± 0.6 mag for SNe Ib and SNe Ic, respectively). In Figure 4, we show a comparison of the SN 2023adta peak brightness (M_R) and light curve $\Delta m_{15,R}$ shape to other SESNe from Drout et al. (2011) and SNe Ic-BL from Taddia et al. (2019). These measurements were derived from *R*- and *r*-band photometry, respectively. Given its sparsely sampled light curve, $\Delta m_{15,R}$ is uncertain but consistent with other SESNe. Its peak brightness is similar to that of other SNe Ic-BL, in particular, those with associated GRBs (blue diamonds with red edges). Using the relationship derived in Drout et al. (2011),

$$\log(M_{\mathrm{Ni}}) \approx -0.41 M_R - 8.3, \quad (1)$$

[we estimate that $M_{\mathrm{Ni}} = 0.3 \pm 0.1\ M_\odot$ for SN 2023adta.

3.2. Spectroscopic Classification and Comparisons

The low resolution of the NIRSpec Prism and uncertainty in underlying contamination from host galaxy light provide additional challenges in the classification of SN 2023adta. The presence of strong host galaxy Hα emission with FWHM $=$ 4000 $\mathrm{km\ s^{-1}}$ could bias classification against SNe II, especially those with relatively narrow emission features like SNe IIn.

Table 4
Best-fit NGSF Parameters for SN 2023adta

Rank	SN	Type	Phase (days)	A_V (mag)	χ^2/ν
1	SN 2006aj	Ic-BL	+16	0.45	3.19
2	SN 2002ap	Ic-BL	+8	1.25	3.42
3	SN 1998bw	Ic-BL	+20	1.90	3.52
4	PTF 10vgv	Ic-BL	+2	2.0	3.93
5	SN 2014G	II	+29	1.2	4.12
8	SN 1994L	Ic	+2	2.0	4.37
10	SN 2013df	IIb	+14	1.0	4.45
11	SN 2015N	Ia	+25	0.0	4.57
21	SN 2006ep	Ib	+11	0.0	5.18

Note. Below the horizontal line, we show the highest rankings for specific SN types.

The spectroscopic classification of SN 2023adta was performed with Next Generation SuperFit[26] (Goldwasser et al. 2022) based on the IDL code Superfit (Howell et al. 2005). This code allows for the simultaneous fitting of the host galaxy light contamination and SN flux. We restrict the fit to use only post-maximum-light template SNe and the "SB1" host galaxy template that best matches the continuum of our host galaxy spectrum (see Figure 2). We also restrict the extinction parameter to 0 mag $< A_V <$ 2 mag. We deredshift the SN spectrum, clip prominent host galaxy emission lines, and then perform NGSF fitting at a resolution of 30 Å. This is similar to the native wavelength binning output by the JWST Stage 3 pipeline, which ranges from 25 to 52 Å across our deredshifted spectrum of SN 2023adta.

A summary of the spectroscopic fitting results is presented in Table 4. Ordered by χ^2/ν, the four best-fit SN spectra are from SNe Ic-BL with phases ranging from +2 to +20 days, in good agreement with the results of our light-curve fit (+11 days). Interestingly, two of these SNe (SN 1998bw and SN 2006aj) have associated GRBs. In each of these fits, the SN contributions are >98%, indicating little host contamination. For SNe Ic-BL, NGSF prefers a high amount of reddening ($A_V > 0.45$ mag), which is consistent with our derived host galaxy parameters ($A_V = 1.8$ mag; see Section 3.4) but not our best-fit light curve ($A_V = 0$ mag). However, we caution that imperfect subtraction of the host galaxy light could strongly influence this parameter. Similar to the light-curve fitting, the second-best-fit SN type is SN II; however, its phase (+29 days) is significantly greater than what we would expect based on the best-fit SN II light curve (+13 days).

Given the limited SN template bank available in NGSF, additional comparisons are needed to provide a secure classification for SN 2023adta. We show spectroscopic matches to SN 2023adta from NGSF along with other useful comparison spectra in Figure 5. For log (f_λ) comparisons, we mask negative values in SN 2023adta that result from imperfect host galaxy subtraction.

From top to bottom, we show our NIRspec Prism spectrum of SN 2023adta in comparison to five SNe Ic-BL (SN 2014ad,

[26] https://github.com/oyaron/NGSF

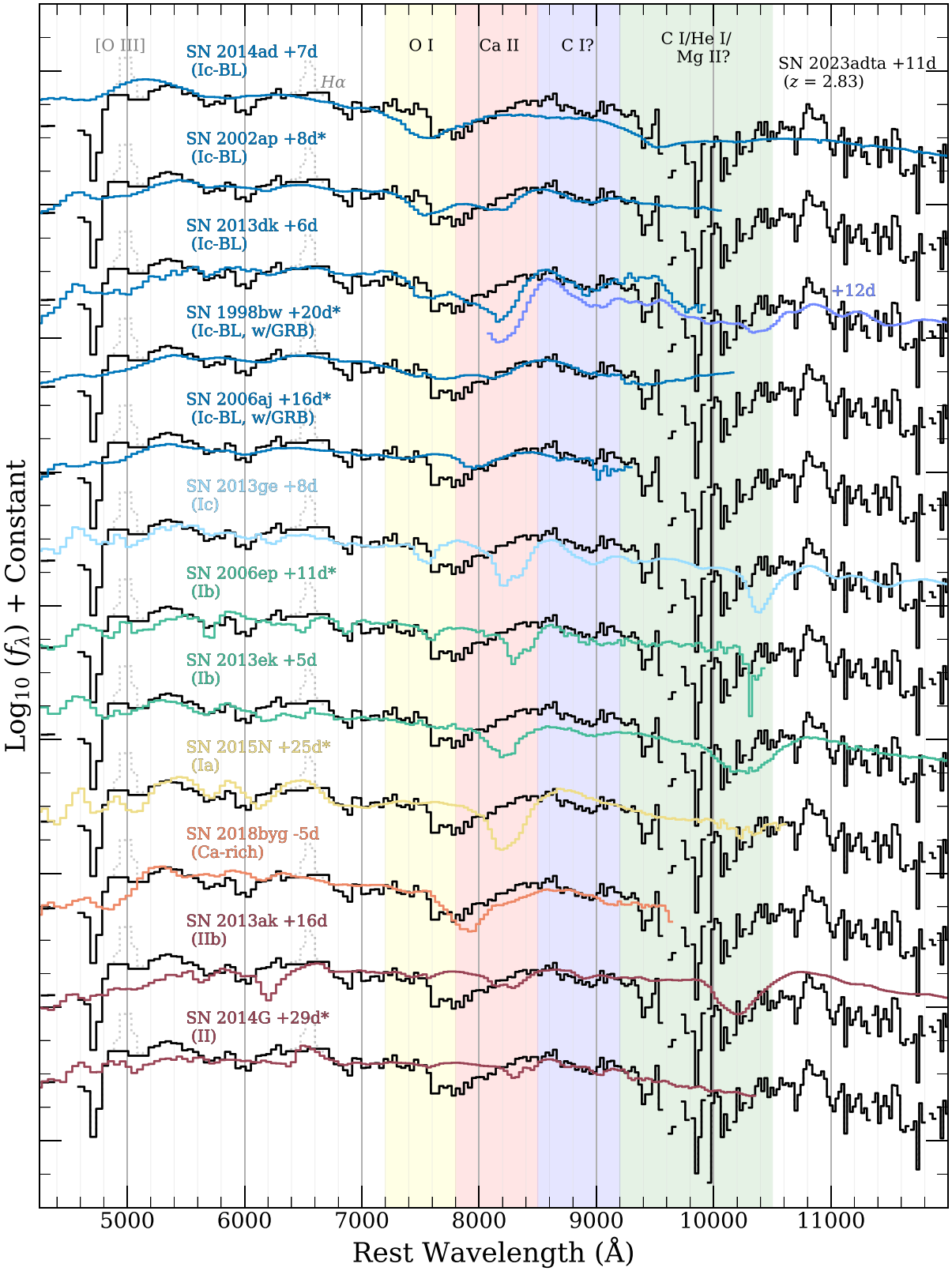

Figure 5. Rest-frame NIRSpec Prism spectrum of SN 2023adta (black curves) compared with spectra of a variety of other SN types at similar phases (colored curves). We mask negative values that result from imperfect host galaxy subtraction. The dotted gray curves show clipped host galaxy emission lines. The color of each curve corresponds to the SN type. From top to bottom, we show five SNe Ic-BL (blue), one SN Ic (light blue), two SNe Ib (green), one SN Ia (yellow), one Ca-rich SN (orange), and one SN IIb (dark red). An asterisk next to the phase of a comparison spectrum indicates that it was a matched spectrum using the SN classification code `NGSF` (Goldwasser et al. 2022).

Kwok et al. 2022; Shahbandeh et al. 2022; SN 2002ap, Mazzali et al. 2002; SN 2013dk, Elias-Rosa et al. 2013; Shahbandeh et al. 2022; SN 1998bw, Galama et al. 1998; and SN 2006aj, Pian et al. 2006), one SN Ic (SN 2013ge, Drout et al. 2016; Shahbandeh et al. 2022), two SNe Ib (SN 2006ep, Smartt et al. 2015; and SN 2013ek, Smartt et al. 2015; Shahbandeh et al. 2022), one SN Ia (SN 2015N, Stahl et al. 2020), one Ca-rich SN (SN 2018byg, De et al. 2019), and one SN IIb (SN 2013ak, Smartt et al. 2015; Shahbandeh et al. 2022). Four of these SNe (SN 2014ad, SN 2013ge, SN 2013ek, and SN 2013ak) have optical spectra that were observed within 1 day of an NIR spectrum presented in Shahbandeh et al. (2022). In these cases, we have combined these data into one full optical-to-NIR spectrum. All comparison spectra have been rebinned to have a similar wavelength spacing to the NIRSpec spectrum of SN 2023adta. We mark spectroscopic fits from NGSF with an asterisk.

There are two primary broad absorption features in the spectrum of SN 2023adta that agree relatively well with other SNe Ic-BL, one at ∼8000 Å and another at ∼10,000 Å. The former is likely produced by the Ca II NIR triplet, and the latter is likely produced from blended contributions from C I, He I, and Mg II (Shahbandeh et al. 2022). Absorption from O I and Ca II can appear as separate features in normal SNe Ic and SNe Ib due to their lower velocities (Matheson et al. 2001). However, in SNe Ic-BL, these features can blend together due to the larger ejecta velocities (Foley et al. 2003). SN Ic-BL comparison spectra in Figure 5 have been selected to showcase the diversity in this wavelength region. Additionally, the spectrum of SN 2013dk at +6 days (+12 in the NIR) exhibits some interesting similarity to SN 2023adta at ∼9000 Å. Shahbandeh et al. (2022) identified this absorption feature as C I in SN 2013dk. This SN also matches the falloff in flux near 4000 Å better than most of the other comparison SNe.

We also make spectroscopic comparisons to normal SESNe and an SN Ia. Generally, these SNe are unable to reproduce the large blueshifts seen in SN 2023adta, and the line strengths relative to the continuum of these SNe are not well matched. The presence of He I and/or Si II in the spectrum of SN 2023adta is ambiguous. SN 2023adta has additional shallow absorption features near 6000 Å that could result from these elements, but the resolution of the data and uncertainty on phase make a definitive line identification in this wavelength region very difficult. Furthermore, He I 10830 Å could contribute to the broad absorption at 10000 Å; however, there is no way to differentiate from potential contributions from C I 10693 Å and/or Mg II 10927 Å (Shahbandeh et al. 2022). Furthermore, for the SN Ia (yellow curve; SN 2015N), NGSF prefers a later phase of +25 days. This could be due to the color of SN 2023adta at the epoch of our spectrum. An SN Ia at an earlier phase, as suggested by the light-curve fit, would likely be too blue to reproduce the observed continuum.

Some peculiar transients like Ca-rich SNe are red at early times due to strong line blanketing (Shen et al. 2018; Polin et al. 2019; Jacobson-Galán et al. 2020). In Figure 5, we show one such event, SN 2018byg (orange curve; De et al. 2019), at −5 days relative to maximum light. This spectrum reproduces the continuum of SN 2023adta well and also has a high Ca II velocity of $-22{,}000\ \mathrm{km\ s^{-1}}$ (De et al. 2019; Jacobson-Galán et al. 2020); however, the strength of this absorption does not match as well as the Ca II features in our SNe Ic-BL comparison spectra. Finally, we compare to an SN IIb and an SN II (dark red curves; SN 2013ak and SN 2014G). These SNe have low ejecta velocities that are difficult to reconcile with SN 2023adta. We measure a Hα FWHM $= 4000\ \mathrm{km\ s^{-1}}$, which is consistent with the resolution of the NIRSpec Prism at this wavelength, indicating that this emission is from the host galaxy. However, a clear continuum is difficult to define in this region, and broader Hα may be present.

Even though there are significant caveats related to both the photometric and spectroscopic classification methods, the observational characteristics of SN 2023adta outlined below provide convincing evidence that it can be classified as an SN Ic-BL at $z = 2.83$.

1. The light-curve fit strongly prefers SN Ib/c, which reproduces the F115W flux at early epochs.
2. NGSF fitting of the NIRSpec spectrum strongly suggests the subclass of SN Ic-BL at a phase consistent with the light curve.
3. Broad, high-velocity absorption features are inconsistent with those observed in normal SNe Ia, Ib, and Ic.
4. Lack of obvious H or He absorption/emission features.
5. Red continuum shape and flux drop-off at rest frame 4000 Å.

3.3. Ejecta Velocity and Physical Parameters

Using a combination of both photometric and spectroscopic properties of SN 2023adta, we can derive some physical parameters of the explosion. Drout et al. (2011) showed how peak luminosity (M_R), light-curve shape ($\Delta m_{15,R}$), and photospheric velocity ($v_{\rm ph}$) are related to the nickel mass ($M_{\rm Ni}$), ejecta mass ($M_{\rm ej}$), and kinetic energy of the explosion ($E_{\rm KE}$). To get an estimate of $v_{\rm ph}$, we examine the Ca II and O I absorption features of SNe Ic-BL in more detail in Figure 6. The spectrum of SN 2014ad reproduces the shape of the primary absorption features well but at larger blueshifts. Kwok et al. (2022) attribute the absorption at ∼7000 Å primarily to O I and estimate a photospheric velocity of $22{,}000\ \mathrm{km\ s^{-1}}$ via a best-fit TARDIS (Kerzendorf et al. 2014) model.

Assuming that the absorption minimum in the spectrum of SN 2023adta is primarily caused by Ca II, using an intensity-weighted rest wavelength of 8567 Å for the Ca II NIR triplet, we estimate an ejecta velocity of $-29{,}000 \pm 2000\ \mathrm{km\ s^{-1}}$, which is consistent with other SNe Ic-BL (Modjaz et al. 2016; Taddia et al. 2019). We find that SN 2023adta may have another weaker absorption feature blueward of Ca II, which, if caused by O I, also indicates ejecta with velocities ranging from 20,000 to $40{,}000\ \mathrm{km\ s^{-1}}$. An estimate of the Fe II 5169 Å line velocity would be a better indicator of the photospheric velocity, since this line does not saturate (Branch et al. 2002; Modjaz et al. 2016); however, the strong residual [O III] emission from the host galaxy prohibits us from making this measurement.

Using the properties of the light curve that we estimated in Section 3.1, we derive physical explosion parameters for SN 2023adta using Equations (1) and (2) and the methods described in Drout et al. (2011). We determine these parameters using our measured Ca II velocity as the photospheric velocity but also calculate results for fiducial velocities of $20{,}000\ \mathrm{km\ s^{-1}}$ and $10{,}000\ \mathrm{km\ s^{-1}}$ for comparison. These parameters are shown in Table 5. We estimate a large ejecta mass and kinetic energy of $5^{+4}_{-2}\,M_\odot$ and $24^{+29}_{-14} \times 10^{51}$ erg, respectively. The large uncertainties primarily arise from the

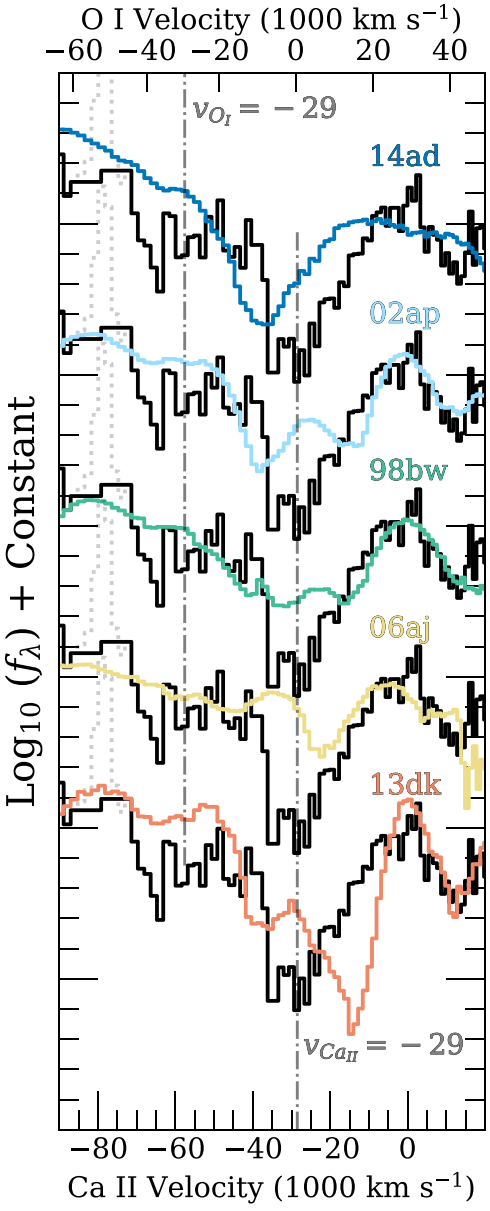

Figure 6. Similar to Figure 5 but zoomed in on the O I and Ca II NIR triplet region of each SN Ic-BL. The velocity width of the primary absorption feature suggests ejecta moving at >20,000 km s^{-1}. The velocity we measure from the absorption minimum is 29,000 ± 2000 km s^{-1}.

poor constraints on the light-curve shape and strong dependence ejecta velocity. Nevertheless, these estimates are consistent with what we expect for engine-driven explosions (Drout et al. 2011; Cano 2013; Taddia et al. 2019).

3.4. Host Galaxy Properties

The presence of an SN Ic-BL at $z = 2.83$ provides a unique opportunity to study the environment of this rare subclass of core-collapse SNe in the early Universe. Its host galaxy is irregular with several bright knots of star formation (see Figure 1). We derive galaxy properties by performing a BAGPIPES (Carnall et al. 2018, 2019) fit to the host galaxy spectrum that was flux-calibrated to the total host flux. From this fit, we find mass $\log_{10}(M_*/M_\odot) = 9.78^{+0.09}_{-0.11}$, stellar metallicity $Z = 0.35^{+0.16}_{-0.08} Z_\odot$, $A_V = 1.832^{+0.10}_{-0.14}$, timescale $\tau = 2.10^{+0.06}_{-0.05}$ Gyr (SFR$\propto e^{t/\tau}$), and redshift $z = 2.833^{+0.002}_{-0.003}$. Assuming a solar metallicity of log(O/H) + 12 = 8.69 (Asplund et al. 2009), we convert the best-fit Z from BAGPIPES to oxygen abundance and find log(O/H) + 12 = $8.23^{+0.16}_{-0.12}$. We caution that this conversion assumes that stellar and gas-phase metallicity are equal.

Table 5
Estimated Explosion Parameters for SN 2023adta

v_{ph} (km s^{-1})	M_{Ni} ($M_\odot$)	M_{ej} ($M_\odot$)	E_{KE} (10^{51} erg)
29,000 ± 2000	0.3 ± 0.1	5^{+4}_{-2}	24^{+29}_{-14}
20,000	0.3 ± 0.1	3^{+3}_{-2}	8^{+11}_{-5}
10,000	0.3 ± 0.1	$1.6^{+1.8}_{-0.9}$	$1.0^{+2.0}_{-0.7}$

We note that the redshift uncertainty from this fit is a factor of 2 larger than that from the Gaussian fitting method discussed in Section 2.3. This method used the highest signal-to-noise ratio emission lines that were close in wavelength relative to the wavelength range of the NIRSpec PRISM. Since BAGPIPES fits over the full wavelength range, there may be additional uncertainties in the wavelength solution that are getting factored into the redshift uncertainty. Furthermore, the NIRSpec PRISM resolution varies by a factor of ∼3 over the entire wavelength range. Since this widens the line-spread function at lower wavelengths, the inclusion of these regions in the fit could also lead to the larger observed uncertainty.

In Figure 7, we compare the mass and metallicity of the host galaxy of SN 2023adta to the mass–metallicity relation of low-z galaxies (Sloan Digital Sky Survey, SDSS, DR8; Eisenstein et al. 2011), high-z galaxies ($z \sim 3$–9; Curti et al. 2023; Nakajima et al. 2023; Morishita et al. 2024), and core-collapse SN host galaxies (Kelly & Kirshner 2012; Modjaz et al. 2020). These data are presented as the gray contours, pink–yellow hexagons, and colored points, respectively. The SDSS and SN host galaxy metallicities were derived via the PP04 O3N2 calibration (Pettini & Pagel 2004), and the metallicities of the high-z galaxies were derived using the direct electron-temperature (T_e) method. We also compare to the mass–metallicity relationship derived for galaxies at $z \sim 3.3$ in the MOSDEF survey (dashed yellow line; Sanders et al. 2021).

We find that the metallicity of the host galaxy of SN 2023adta is in good agreement with those of other SN Ic-BL host galaxies (dark blue diamonds). This corroborates previous work that has determined that these high-energy events tend to occur in lower-metallicity environments than those of other SESNe and normal core-collapse SNe (Kelly & Kirshner 2012; Sanders et al. 2012; Modjaz et al. 2020). In particular, our measured metallicity for SN 2023adta is very similar to the mean SN Ic-BL PP04 O3N2 metallicity, log(O/H) + 12 = 8.31 ± 0.04, and mean SN-GRB PP04 O3N2 metallicity, log(O/H) + 12 = 8.20 ± 0.06, reported in Modjaz et al. (2020). Furthermore, both the mass and metallicity of the host galaxy of SN 2023adta are consistent with what we expect for galaxies at this redshift. Given their rarity (∼4% of the rate of core-collapse SNe by volume; Shivvers et al. 2017), the likelihood of observing an SN Ic-BL in the JADES DDT sample is small. However, since the metallicities of high-z galaxies are lower, it is possible that SNe Ic-BL occur at an enhanced rate at higher redshifts. We note that the mean galaxy mass of the SN Ic-BL host galaxies displayed is $\log_{10}(M_*/M_\odot) = 9.1$ with a standard deviation of 0.8. SN 2023adta has a relatively high host galaxy mass, $\log_{10}(M_*/M_\odot) = 9.78^{+0.09}_{-0.11}$. However, SN 2023adta was

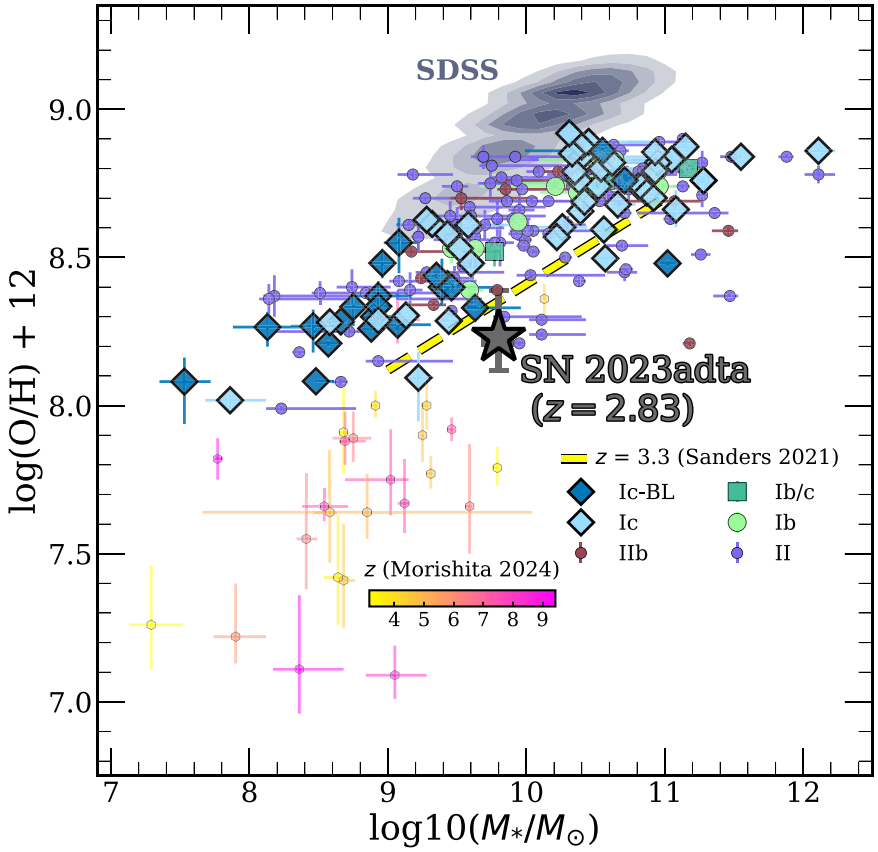

Figure 7. A comparison of the host galaxy properties of SN 2023adta to the mass–metallicity relationship observed in SDSS field galaxies (gray contours, $z \sim 0$; Eisenstein et al. 2011), core-collapse SN host galaxies from Kelly & Kirshner (2012) and additional SN Ic/Ic-BL host galaxies from Modjaz et al. (2020; colored points), and high-z galaxies observed with JWST (pink–yellow hexagons; Morishita et al. 2024). The dashed yellow line is the empirical, $z = 3.3$, mass–metallicity relationship derived in Sanders et al. (2021).

not discovered in an untargeted survey like the majority of SNe Ic-BL displayed. Since the presence of a clear host galaxy was used to motivate its spectroscopic follow-up, there could be a significant selection effect in the JADES SN sample for SNe in more massive host galaxies.

3.5. Searching for Coincident GRBs with SN 2023adta

The connection between SNe Ic-BL and LGRBs would be interesting to constrain at high z. We used the online database GRBWeb[27] to search for spatially and temporally coincident GRBs that could be associated with SN 2023adta. We find that the best candidate for an associated GRB is GRB 230911A. The MJD of this event was 60198, 66 days prior to our first detection of SN 2023adta. Based on our best-fit light curve, this GRB occurred at a phase of −18 days. The location of this GRB (R.A. = 59.8, decl. = −34.4; GCN Circular 34652[28]) is 4.°3 from SN 2023adta with an uncertainty of 4°.1. However, GRB 230911A also has an associated optical afterglow, GOTO 23akf/AT 2023shv (Belkin et al. 2024), at R.A. = $3^{h}50^{m}0\overset{s}{.}51$, decl. = $-29^{d}49^{m}30\overset{s}{.}66$ with $0\overset{''}{.}3$ uncertainty. With a separation of 4.°3 from SN 2023adta, we conclude that GRB 230911A is not associated with this SN. Furthermore, a Swift-XRT afterglow was also detected (GCN Circular 34702[29]) at R.A. = $3^{h}50^{m}0\overset{s}{.}65$, decl. = $-29^{d}49^{m}33\overset{s}{.}2$ with $3\overset{''}{.}4$ uncertainty, providing additional support for this conclusion. We do not find any other GRBs that are likely to be spatially and temporally coincident with SN 2023adta.

4. Discussion and Conclusions

As part of a DDT follow-up program for the JADES Transient Survey (D24), we used JWST NIRCam and NIRSpec observations to confirm the presence of an SN Ic at $z = 2.83$ (SN 2023adta). To date, this is the most distant SESN ever discovered, occurring when the age of the Universe was approximately 2.2 Gyr. Analysis of the light curve and spectrum of SN 2023adta provides strong evidence that this SN fits within the SN Ic-BL subclass of SESNe. These SNe are characterized by their broad absorption features indicating typical ejecta velocities of ∼20,000–30,000 km s^{-1}, high explosion energies, and lack of H and He features and have been associated with LGRBs. This subclass also has a preference for low-metallicity environments relative to other SESNe (Kelly & Kirshner 2012; Sanders et al. 2012; Modjaz et al. 2020).

SN 2023adta satisfies many of these criteria. First, we fit the observed light curve and found a best-fit photometric classification of SN Ib/c. In particular, this model reproduces the flux in F115W better than any other SN type. Our best fit indicates that the phase of NIRSpec observation is at ∼+11 days. While it is difficult to distinguish SN Ib/c/c-BL using solely the light-curve shape, we find that SN 2023adta had a peak luminosity in $M_V = -19.0 \pm 0.2$. This is consistent

[27] https://user-web.icecube.wisc.edu/~grbweb_public/index.html
[28] https://gcn.nasa.gov/circulars/34652
[29] https://gcn.nasa.gov/circulars/34702

with the high luminosities observed in SNe Ic-BL relative to other SESNe (Drout et al. 2011; Cano 2013; Taddia et al. 2019), and the high peak luminosity of the best-fit SN II models, $M_V = -19.4 \pm 0.3$, is inconsistent with the luminosity distribution of normal SN II. Furthermore, engine-driven explosions, the subset of SNe Ic-BL characterized by their associations with LGRBs, tend to have the highest luminosities within the SN Ic-BL subclass (Drout et al. 2011; Taddia et al. 2019).

Second, we performed spectroscopic classification of SN 2023adta on our NIRSpec Prism spectrum using the fitting code `NGSF` based on the IDL code Superfit (Howell et al. 2005). This code models contributions from the SN and host galaxy and found results consistent with our photometric classification. SN 2023adta has broad absorption features in the optical and NIR that are consistent with those observed in SNe Ic-BL. The absorption feature at a rest wavelength of ~8000 Å is likely produced by the Ca II NIR triplet and implies ejecta velocities of $\sim$29,000 km s^{-1}, in agreement with the large explosion energy that we infer from the light curve. Additionally, we do not find strong evidence for H or He features that would be typical for normal SNe Ib or SNe II. In combination with the light-curve properties of SN 2023adta, we estimate nickel mass, ejecta mass, and kinetic energy ($0.3 \pm 0.1\,M_\odot$, $5^{+4}_{-2}\,M_\odot$, and $24^{+29}_{-14} \times 10^{51}$) that are consistent with typical values for SNe Ic-BL (Taddia et al. 2019).

Third, we estimated properties of the host galaxy of SN 2023adta and found that its metallicity is low relative to other core-collapse SNe observed in the local Universe. This is in agreement with previous analyses of SN Ic-BL host galaxies and what is expected for the galaxy mass–metallicity relationship at $z = 2.83$. Lastly, we do not identify any GRBs that are coincident with SN 2023adta.

SNe Ic-BL are rare in the local Universe (~4% of the core-collapse SN rate; Shivvers et al. 2017); therefore, detection of an SN Ic-BL at $z = 2.83$ within a small sample suggests that the rate of these events may be enhanced at this distance. Future observations are needed to constrain the rates of these SNe at high z and to understand how their host populations may or may not evolve with redshift.

JWST is a remarkable tool for this task and, in general, the characterization of the high-z transient Universe. The NIRSpec MOS mode is capable of observing several candidate SNe at once, making it very efficient for transient follow-up and classification. The work presented here highlights some additional challenges that the community will face as a sample of high-z SNe continues to be constructed. Specifically, at these distances, it can become very difficult to separate light from an SN and its host galaxy. Host galaxy continuum contamination can make SN features appear weak and difficult to distinguish, and at low resolution (like the NIRSpec Prism), galaxy emission line contamination can preclude the identification of key SN features (e.g., broad Hα). Future high-z transient survey design should consider these limitations and take steps to mitigate their impact. Furthermore, the Nancy Grace Roman Space Telescope will also include only a low-resolution dispersive element, and SN classification will be similarly difficult. More work is needed to improve classification at low resolution in order to get the most out of future high-z SNe observed with these telescopes.

Acknowledgments

This work is based on observations made with the NASA/ESA/CSA JWST as part of programs 1180 and 6541. Support for program JWST-GO-06541 was provided by NASA through a grant from the Space Telescope Science Institute, which is operated by the Association of Universities for Research in Astronomy, Inc., under NASA contract NAS 5-03127. This Letter is based on observations with the NASA/ESA Hubble Space Telescope and James Webb Space Telescope obtained from the Mikulski Archive for Space Telescopes at STScI. We thank the DDT and JWST/HST scheduling teams and instrument experts at STScI for extraordinary effort in getting the DDT observations used here scheduled quickly.

M.R.S. is supported by an STScI Postdoctoral Fellowship. J.D.R.P. is supported by NASA through Einstein Fellowship grant No. HF2-51541.001 awarded by the Space Telescope Science Institute (STScI), which is operated by the Association of Universities for Research in Astronomy, Inc., for NASA, under contract NAS5-26555. This research is based (in part) on observations made with the NASA/ESA Hubble Space Telescope obtained from the Space Telescope Science Institute, which is operated by the Association of Universities for Research in Astronomy, Inc., under NASA contract NAS 526555. The JWST data used in this Letter can be found in MAST at doi:10.17909/ftmd-s562.

Additionally, this work made use of the *lux* supercomputer at UC Santa Cruz, which is funded by NSF MRI grant AST 1828315, as well as the High Performance Computing (HPC) resources at the University of Arizona, which are funded by the Office of Research Discovery and Innovation (ORDI), Chief Information Officer (CIO), and University Information Technology Services (UITS). A.J.B. acknowledges funding from the "FirstGalaxies" Advanced Grant from the European Research Council (ERC) under the European Union's Horizon 2020 research and innovation program (grant agreement No. 789056).

P.A.C., E.E., D.J.E., and B.D.J. are supported by a JWST/NIRCam contract to the University of Arizona, NAS5-02015. D.J.E. is also supported as a Simons Investigator. R.M. acknowledges support by the Science and Technology Facilities Council (STFC), the ERC through Advanced grant 695671 "QUENCH", and the UKRI Frontier Research grant RISEandFALL. R.M. also acknowledges funding from a research professorship from the Royal Society.

B.E.R. acknowledges support from the NIRCam Science Team contract to the University of Arizona, NAS5-02015, and JWST Program 3215. J.D.R.P. is supported by NASA through Einstein Fellowship grant No. HF2-51541.001 awarded by the Space Telescope Science Institute (STScI), which is operated by the Association of Universities for Research in Astronomy, Inc., for NASA, under contract NAS5-26555. Y.Z. thanks Matteo Cantiello for helpful discussions.

Facility: JWST (NIRCam/NIRSpec).

Software: astropy (Astropy Collaboration et al. 2013, 2018, 2022)

ORCID iDs

M. R. Siebert https://orcid.org/0000-0003-2445-3891
C. DeCoursey https://orcid.org/0000-0002-4781-9078
D. A. Coulter https://orcid.org/0000-0003-4263-2228
M. Engesser https://orcid.org/0000-0003-0209-674X

J. D. R. Pierel https://orcid.org/0000-0002-2361-7201
A. Rest https://orcid.org/0000-0002-4410-5387
E. Egami https://orcid.org/0000-0003-1344-9475
M. Shahbandeh https://orcid.org/0000-0002-9301-5302
W. Chen https://orcid.org/0000-0003-1060-0723
O. D. Fox https://orcid.org/0000-0003-2238-1572
Y. Zenati https://orcid.org/0000-0002-0632-8897
T. J. Moriya https://orcid.org/0000-0003-1169-1954
A. J. Bunker https://orcid.org/0000-0002-8651-9879
P. A. Cargile https://orcid.org/0000-0002-1617-8917
M. Curti https://orcid.org/0000-0002-2678-2560
D. J. Eisenstein https://orcid.org/0000-0002-2929-3121
S. Gezari https://orcid.org/0000-0003-3703-5154
S. Gomez https://orcid.org/0000-0001-6395-6702
M. Guolo https://orcid.org/0000-0002-5063-0751
B. D. Johnson https://orcid.org/0000-0002-9280-7594
B. A. Joshi https://orcid.org/0000-0002-7593-8584
M. Karmen https://orcid.org/0000-0003-2495-8670
R. Maiolino https://orcid.org/0000-0002-4985-3819
R. M. Quimby https://orcid.org/0000-0001-9171-5236
B. Robertson https://orcid.org/0000-0002-4271-0364
L. G. Strolger https://orcid.org/0000-0002-7756-4440
F. Sun https://orcid.org/0000-0002-4622-6617
Q. Wang https://orcid.org/0000-0001-5233-6989
T. Wevers https://orcid.org/0000-0002-4043-9400

References

Anderson, J. P., Dessart, L., Gutiérrez, C. P., et al. 2018, NatAs, 2, 574
Arcavi, I. 2018, ApJL, 855, L23
Arcavi, I., Gal-Yam, A., Kasliwal, M. M., et al. 2010, ApJ, 721, 777
Asplund, M., Grevesse, N., Sauval, A. J., & Scott, P. 2009, ARA&A, 47, 481
Astropy Collaboration, Price-Whelan, A. M., Lim, P. L., et al. 2022, ApJ, 935, 167
Astropy Collaboration, Price-Whelan, A. M., Sipőcz, B. M., et al. 2018, AJ, 156, 123
Astropy Collaboration, Robitaille, T. P., Tollerud, E. J., et al. 2013, A&A, 558, A33
Barnes, J., Duffell, P. C., Liu, Y., et al. 2018, ApJ, 860, 38
Becker, A. 2015, HOTPANTS: High Order Transform of PSF ANd Template Subtraction, Astrophysics Source Code Library, ascl:1504.004
Belkin, S., Gompertz, B. P., Kumar, A., et al. 2024, RNAAS, 8, 6
Branch, D., Benetti, S., Kasen, D., et al. 2002, ApJ, 566, 1005
Bunker, A. J., Cameron, A. J., Curtis-Lake, E., et al. 2023, arXiv:2306.02467
Bushouse, H., Eisenhamer, J., Dencheva, N., et al. 2024, JWST Calibration Pipeline, v1.14.0, Zenodo, doi:10.5281/zenodo.7038885
Cano, Z. 2013, MNRAS, 434, 1098
Cao, Y., Kasliwal, M. M., Arcavi, I., et al. 2013, ApJL, 775, L7
Carnall, A. C., Leja, J., Johnson, B. D., et al. 2019, ApJ, 873, 44
Carnall, A. C., McLure, R. J., Dunlop, J. S., & Davé, R. 2018, MNRAS, 480, 4379
Clocchiatti, A., Wheeler, J. C., Benetti, S., & Frueh, M. 1996, ApJ, 459, 547
Corsi, A., Ofek, E. O., Gal-Yam, A., et al. 2012, ApJL, 747, L5
Curti, M., D'Eugenio, F., Carniani, S., et al. 2023, MNRAS, 518, 425
De, K., Kasliwal, M. M., Polin, A., et al. 2019, ApJL, 873, L18
DeCoursey, C., Egami, E., Pierel, J. D. R., et al. 2024, arXiv:2406.05060
Dessart, L., Hillier, D. J., Li, C., & Woosley, S. 2012, MNRAS, 424, 2139
Dessart, L., Yoon, S.-C., Aguilera-Dena, D. R., & Langer, N. 2020, A&A, 642, A106
Developers, J., Averbukh, & Bradley, J. 2023, Jdaviz: JWST Astronomical Data Analysis Tools in the Jupyter Platform, Astrophysics Source Code Library, ascl:2307.001
Drout, M. R., Soderberg, A. M., Gal-Yam, A., et al. 2011, ApJ, 741, 97
Drout, M. R., Milisavljevic, D., Parrent, J., et al. 2016, ApJ, 821, 57
Eisenstein, D. J., Weinberg, D. H., Agol, E., et al. 2011, AJ, 142, 72
Eisenstein, D. J., Willott, C., Alberts, S., et al. 2023, arXiv:2306.02465
Eldridge, J. J., & Maund, J. R. 2016, MNRAS, 461, L117
Elias-Rosa, N., Pastorello, A., Maund, J. R., et al. 2013, MNRAS, 436, L109
Ferruit, P., Jakobsen, P., Giardino, G., et al. 2022, A&A, 661, A81
Filippenko, A. V., Barth, A. J., Bower, G. C., et al. 1995, AJ, 110, 2261
Folatelli, G., Van Dyk, S. D., Kuncarayakti, H., et al. 2016, ApJL, 825, L22
Foley, R. J., Papenkova, M. S., Swift, B. J., et al. 2003, PASP, 115, 1220
Fox, O. D., Van Dyk, S. D., Williams, B. F., et al. 2022, ApJL, 929, L15
Gagliano, A., Izzo, L., Kilpatrick, C. D., et al. 2022, ApJ, 924, 55
Gal-Yam, A. 2017, in Handbook of Supernovae, ed. A. W. Alsabti & P. Murdin (Berlin: Springer), 195
Galama, T. J., Vreeswijk, P. M., van Paradijs, J., et al. 1998, Natur, 395, 670
Georgy, C., Meynet, G., Walder, R., Folini, D., & Maeder, A. 2009, A&A, 502, 611
Goldwasser, S., Yaron, O., Sass, A., et al. 2022, TNSAN, 191, 1
Gutiérrez, C. P., Anderson, J. P., Sullivan, M., et al. 2018, MNRAS, 479, 3232
Howell, D. A., Sullivan, M., Perrett, K., et al. 2005, ApJ, 634, 1190
Iwamoto, K., Brachwitz, F., Nomoto, K., et al. 1999, ApJS, 125, 439
Jacobson-Galán, W. V., Polin, A., Foley, R. J., et al. 2020, ApJ, 896, 165
Jakobsen, P., Ferruit, P., Alves de Oliveira, C., et al. 2022, A&A, 661, A80
Janka, H.-T., Melson, T., & Summa, A. 2016, ARNPS, 66, 341
Kelly, P. L., & Kirshner, R. P. 2012, ApJ, 759, 107
Kerzendorf, W. E., Taubenberger, S., Seitenzahl, I. R., & Ruiter, A. J. 2014, ApJL, 796, L26
Kilpatrick, C. D., Drout, M. R., Auchettl, K., et al. 2021, MNRAS, 504, 2073
Kwok, L. A., Williamson, M., Jha, S. W., et al. 2022, ApJ, 937, 40
Li, W., Leaman, J., Chornock, R., et al. 2011, MNRAS, 412, 1441
Lyman, J. D., Bersier, D., James, P. A., et al. 2016, MNRAS, 457, 328
Maeda, K., Mazzali, P. A., Deng, J., et al. 2003, ApJ, 593, 931
Mannucci, F., Salvaterra, R., & Campisi, M. A. 2011, MNRAS, 414, 1263
Matheson, T., Filippenko, A. V., Li, W., Leonard, D. C., & Shields, J. C. 2001, AJ, 121, 1648
Mazzali, P. A., Deng, J., Maeda, K., et al. 2002, ApJL, 572, L61
Milisavljevic, D., Margutti, R., Parrent, J. T., et al. 2015, ApJ, 799, 51
Modjaz, M., Liu, Y. Q., Bianco, F. B., & Graur, O. 2016, ApJ, 832, 108
Modjaz, M., Stanek, K. Z., Garnavich, P. M., et al. 2006, ApJL, 645, L21
Modjaz, M., Bianco, F. B., Siwek, M., et al. 2020, ApJ, 892, 153
Morishita, T., Stiavelli, M., Grillo, C., et al. 2024, ApJ, 971, 43
Nakajima, K., Ouchi, M., Isobe, Y., et al. 2023, ApJS, 269, 33
Pettini, M., & Pagel, B. E. J. 2004, MNRAS, 348, L59
Pian, E., Mazzali, P. A., Masetti, N., et al. 2006, Natur, 442, 1011
Pierel, J. D. R., Engesser, M., Coulter, D. A., et al. 2024a, ApJL, 971, L32
Pierel, J. D. R., Frye, B. L., Pascale, M., et al. 2024b, ApJ, 967, 50
Pierel, J. D. R., Jones, D. O., Kenworthy, W. D., et al. 2022, ApJ, 939, 11
Pierel, J. D. R., Rodney, S., Avelino, A., et al. 2018, PASP, 130, 114504
Podsiadlowski, P., Joss, P. C., & Hsu, J. J. L. 1992, ApJ, 391, 246
Polin, A., Nugent, P., & Kasen, D. 2019, ApJ, 873, 84
Prentice, S. J., Mazzali, P. A., Pian, E., et al. 2016, MNRAS, 458, 2973
Rest, A., Pierel, J., Correnti, M., et al. 2023, arminrest/jhat: The JWST HST Alignment Tool (JHAT), v2, Zenodo, doi:10.5281/zenodo.7892935
Riess, A. G., Macri, L. M., Hoffmann, S. L., et al. 2016, ApJ, 826, 56
Riess, A. G., Casertano, S., Yuan, W., et al. 2018, ApJ, 861, 126
Sahu, D. K., Anupama, G. C., Chakradhari, N. K., et al. 2018, MNRAS, 475, 2591
Sana, H., de Mink, S. E., de Koter, A., et al. 2012, Sci, 337, 444
Sanders, N. E., Soderberg, A. M., Levesque, E. M., et al. 2012, ApJ, 758, 132
Sanders, R. L., Shapley, A. E., Jones, T., et al. 2021, ApJ, 914, 19
Shahbandeh, M., Hsiao, E. Y., Ashall, C., et al. 2022, ApJ, 925, 175
Shen, K. J., Kasen, D., Miles, B. J., & Townsley, D. M. 2018, ApJ, 854, 52
Shivvers, I., Modjaz, M., Zheng, W., et al. 2017, PASP, 129, 054201
Smartt, S. J., Valenti, S., Fraser, M., et al. 2015, A&A, 579, A40
Smith, N., Mauerhan, J. C., Cenko, S. B., et al. 2015, MNRAS, 449, 1876
Stahl, B. E., Zheng, W., de Jaeger, T., et al. 2020, MNRAS, 492, 4325
Sun, N.-C., Maund, J. R., Crowther, P. A., et al. 2022, MNRAS, 510, 3701
Taddia, F., Sollerman, J., Leloudas, G., et al. 2015, A&A, 574, A60
Taddia, F., Moquist, P., Sollerman, J., et al. 2016, A&A, 587, L7
Taddia, F., Sollerman, J., Fremling, C., et al. 2019, A&A, 621, A71
Tucker, M. A., Hinkle, J., Angus, C. R., et al. 2024, arXiv:2405.00113
Valenti, S., Howell, D. A., Stritzinger, M. D., et al. 2016, MNRAS, 459, 3939
Van Dyk, S. D., de Mink, S. E., & Zapartas, E. 2016, ApJ, 818, 75
Woosley, S. E. 1993, ApJ, 405, 273
Woosley, S. E., & Bloom, J. S. 2006, ARA&A, 44, 507
Woosley, S. E., Eastman, R. G., Weaver, T. A., & Pinto, P. A. 1994, ApJ, 429, 300
Woosley, S. E., & MacFadyen, A. I. 1999, A&AS, 138, 499
Woosley, S. E., & Weaver, T. A. 1995, ApJS, 101, 181
Yoon, S. C., Woosley, S. E., & Langer, N. 2010, ApJ, 725, 940
Zapartas, E., de Mink, S. E., Van Dyk, S. D., et al. 2017, ApJ, 842, 125
Zenati, Y., Siegel, D. M., Metzger, B. D., & Perets, H. B. 2020, MNRAS, 499, 4097